Asress Mulugeta Biadgo

PhD Student
Addis Ababa University
Technology Faculty
Department of Mechanical Engineering
Addis Ababa
Ethiopia

Aleksandar Simonovic

Associate Professor
University of Belgrade
Faculty of Mechanical Engineering

Jelena Svorcan

Teaching Assistant
University of Belgrade
Faculty of Mechanical Engineering

Slobodan Stupar

Full Professor
University of Belgrade
Faculty of Mechanical Engineering

Aerodynamic Characteristics of High Speed Train under Turbulent Cross Winds: a Numerical Investigation using Unsteady-RANS Method

Increasing velocity combined with reduced mass of modern high speed trains poses the question of influence of strong cross winds on its aerodynamics. Strong cross winds may affect the running stability of high speed trains via the amplified aerodynamic forces and moments. In this study, simulations of turbulent cross wind flows over the leading and end car of ICE-2 high speed train have been performed at different yaw angles The train aerodynamic problems are closely associated with the flows occurring around train. The flow around the train has been considered as incompressible and was obtained by solving the incompressible form of the unsteady Reynolds-Averaged Navier-Stokes (RANS) equations combined with the realizable k-epsilon turbulence model. Important aerodynamic coefficients such as the side force and rolling moment coefficients have been calculated for yaw angles ranging from -30° to 60° and compared to results obtained from wind tunnel tests. The dependence of the flow structure on yaw angle has also been presented.

Keywords: *cross-wind, high speed trains, computational fluid dynamics, Reynolds-averaged Navier-Stokes equations, k-epsilon turbulence model, numerical analysis.*

1. BACKGROUND AND MOTIVATION

Railway transport is widely used in many countries. Recently, the Ethiopian government has given the Ethiopian Railways Corporation (ERC) the task of developing a national railway network. To date Ethiopia has rail transport system which consists of only 781km of old French-built railway from the Red Sea port Djibouti to Addis Ababa. This old French built railway is currently under construction to be replaced by a Chinese-built standard gauge electrified railway. According to ERC, the new electric trains with design speed of 160km/h will be used for freight and passenger transport, replacing slow and costly truck transport. In addition, the Ethiopian government has considered constructing a series of eight rail network corridors (Fig.1) totalling 4,744km in two phases, with the aim of creating a series of key trade routes to neighbouring Kenya, South Sudan, Sudan and Djibouti. The construction of railway is a key component of the Ethiopia's government plan to boost economic growth and enhance regional integration.

The development of railway transportation and the increase in train speed result in significant social and economic benefits. Western Europe dominates the market, followed by Asia and the Pacific. In October 1964, in Japan, the first high-speed rail in the world was put into operation with the highest speed of 210km/h [1]. Since then, during the last decades, there has been

rapid development of high speed rail system in many countries such as Germany, France, Italy, Spain, China and South Korea. In addition to these, other emerging countries like Turkey and Brazil are also constructing high speed rail networks to connect their major cities. Some African countries such as Morocco, Algeria and South Africa proposed to build a combined passenger and freight high speed railway.
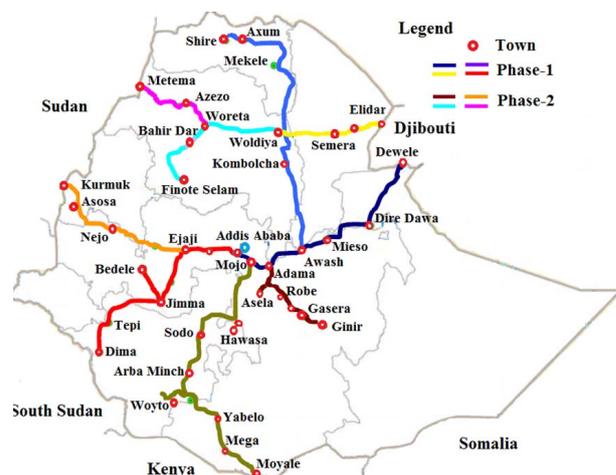
Figure 1. Planned and ongoing rail way network in Ethiopia

Many of the current generation high speed trains such as the Spanish AVE class 103, the German ICE-3, the French TGV Duplex, the South Korean KTX-II, the Chinese CHR C, and the Japanese Shinkansen E6 reach speeds of 300km/h in regular operation. At these speeds aerodynamic forces and moments are becoming more and more important for the running performance of the train. Strong cross wind may affect the running stability and riding comfort of the vehicles.

The increases of the aerodynamic forces and moments due to cross winds may deteriorate the train operating safety and cause the train to overturn. The stability of trains in cross winds is a great concern to a number of countries with high-speed rail networks [2]. Crosswind stability of rail vehicles has been a research topic during the last decades, mainly motivated by overturning accidents. Therefore, understanding of train stability under crosswinds should be a topic of recognized safety issue in the railway community of every country. Recently, the aerodynamics of a train under the influence of cross winds has become a relevant safety topic which is covered in national standards in the UK [3], in Italy [4], in Germany [5] as well as in the European Community legislation and norm [6-7].

The risk of cross wind induced overturning depends on both the track infrastructure and the vehicles aerodynamic characteristics [8]. On the infrastructure side, sites with tall viaducts and high embankments call for attention. The combination of modern light weight and high speed leads to an increased concern regarding the stability of high-speed trains, especially when travelling on high embankments exposed to crosswinds and sudden, powerful wind gusts. Therefore, acquiring detailed and correct data on these scenarios is quite important due to the involved risks of accidents such as a train overturning.

On the vehicles side, the topic of train overturning due to cross wind exposure is closely linked to the susceptibility to cross winds of the leading car of the train set, which is often the most sensitive part. This is because the front-end of a railway car is usually subjected to the largest aerodynamic loads per unit length [9-10].
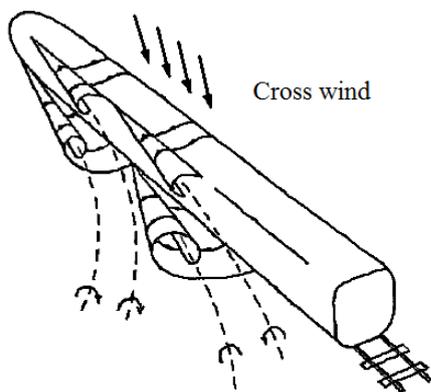
Figure 2. Flow behind a train in a cross wind

The crosswind stability against overturning is a major design criterion for high speed railway vehicles and has been an experimental and/or numerical research topic for a number of scholars [11-18]. The experimental study allows to have a higher confidence in the absolute values of the measured aerodynamic forces whereas the numerical calculations allow to obtain a more detailed information of the flow field around the vehicle.

Among the experimental investigators, Alexander Orellano and Martin Schober [14] have conducted a wind tunnel experiments on the aerodynamic performance of a generic high-speed train. The wind tunnel model used was a simplified 1:10 scaled ICE-2 train with and without simplified bogies. The model is known as Aerodynamic Train Model (ATM). The study involved the application of steady aerodynamic loads on the stationary first car of the ATM for flat ground scenario at yaw angles ranging from -30° to 60°. The flow speed considered was 70m/s, which corresponds to Reynolds numbers of 1.4×10^6 based on the approximate model width of the train (0.3m). The results have been presented through aerodynamic coefficients.

The objective of this study is to conduct a numerical investigation using unsteady RANS method combined with the k-epsilon turbulence model on the aerodynamic characteristics of the leading and end car of ICE-2 high speed train subjected to a cross-wind. The width, length and height of the modeled train are 3m, 29.3m and 3.9m respectively. Similar to the experimental set up, in this paper, the numerical simulation scenario consists of a stationary train model exposed to a constant cross wind of 70m/s at different yaw angles ranging from -30° to 60°. The results were compared to the wind tunnel experimental data [14].

At present, feasible modeling technologies for turbulent flows are steady and unsteady RANS methods, Large Eddy Simulation (LES) and Detached Eddy Simulation (DES). Because of its relatively low computational cost, the unsteady RANS method was used in this study. The aim is to assess the predicting capability of the unsteady RANS method by examining the behavior of the vehicle's aerodynamic coefficients numerically and comparing to the wind tunnel results.

This paper is arranged in such a way that section two aims merely to be a short review of the derivation of the continuity and Navier-Stokes equations. In sections three and four, the numerical simulation method and results will be discussed respectively.

2. THEORY

The equations which govern the flow over the train are the continuity and Navier-Stokes equations. These equations are nothing but the mathematical statements of two fundamental physical principles which are conservation of mass and Newton's second low [19]. In this section, those governing equations will be derived by applying physical principles to a suitable model of the flow.

2.1 Continuity equation

Consider a specific mass of fluid whose volume V is arbitrarily chosen (see Fig. 3). If this given fluid mass is followed as it moves, its size and shape may change but its mass will remain unchanged. Hence, one can state that the time-rate-of-change of the integral of the mass of the fluid element is zero as the element moves along with the flow.

$$\frac{D}{Dt} \int_V \rho dV = 0 \qquad (1)$$

where ρ and t are density and time respectively. Applying Reynolds' transport theorem [20] and divergence theorem to the above equation one obtains:

$$\int_V \left[\frac{\partial \rho}{\partial t} + \nabla \cdot (\rho \vec{u}) \right] dV = 0 \qquad (2)$$

where $\vec{u}(u,v,w)$ is the flow velocity vector field. Since the volume V was arbitrarily chosen, the only way in which the equation (2) can be satisfied for all possible choices of V is for the integrand to be zero. Then equation expressing conservation of mass will be given as:

$$\frac{\partial \rho}{\partial t} + \nabla \cdot (\rho \vec{u}) = 0. \qquad (3)$$

Equation (3) is the differential form of the continuity equation for compressible fluid.
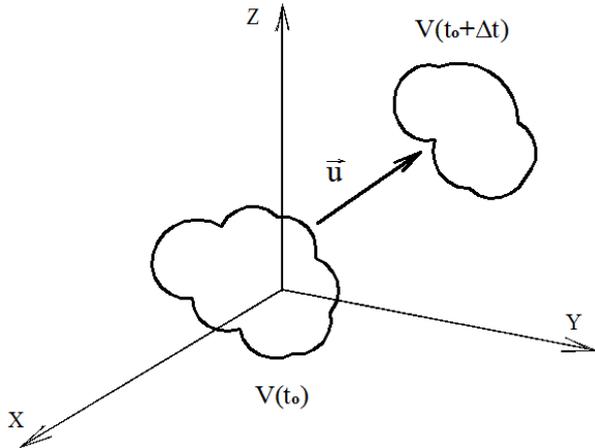
Figure 3. Arbitrary material volume at times t and t+Dt

2.2 Momentum equation

Consider the flow model of a moving fluid element with only the forces in the *x* direction shown (see Fig. 4). When Newton's second law applied to the moving fluid element states that the net force on the fluid element equals its mass times the acceleration of the element, $F_x = ma_x$. This is a vector relation, and hence can be split into three scalar relations along the *x*, *y*, and *z*-axes.
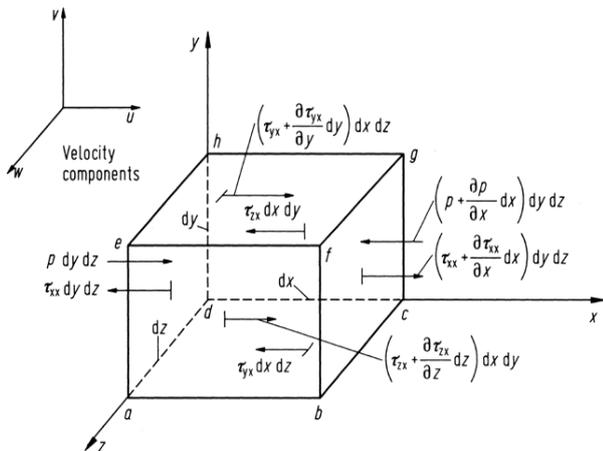
Figure 4. Infinitesimal moving fluid element

The moving fluid element experiences a force in the *x*-direction due to body forces and surface forces. The body forces act at a distance directly on the volumetric mass of the fluid element. Examples are gravitational, electric and magnetic forces. Whereas the surface forces

which act directly along the surface of the fluid element are due to only two sources: (a) the pressure distribution acting on the surface, imposed by the outside fluid surrounding the fluid element, and (b) the shear and normal stress distributions acting on the surface, also imposed by the outside fluid 'tugging' or 'pushing' on the surface by means of friction.

If the body force per unit mass acting on the fluid element is denoted by $\vec{f}$, with f_x as its x-component and the volume of the fluid element is (dxdydz), the body force on the fluid element acting in the x-direction will be ρf_x(dxdydz). Adding all the net surface forces in the x-direction in Fig. 4 together with the body force in the x-direction, the total force in the *x*-direction, F_x, will be:

$$F_x = \left(\left(-\frac{\partial p}{\partial x} + \frac{\partial \tau_{xx}}{\partial x} + \frac{\partial \tau_{yx}}{\partial y} + \frac{\partial \tau_{zx}}{\partial z} \right) + \rho f_x \right) dxdydz. \qquad (4)$$

The mass of the fluid element is fixed and is equal to ρ(dxdydz) and the acceleration of the fluid element is nothing but the time-rate-of-change of its velocity ($a_x = Du/Dt$) in the *x*-direction. Now by applying Newton's second law ($F_x = ma_x$), the *x*-component of the momentum equation for a viscous flow will be:

$$\rho \frac{Du}{Dt} = -\frac{\partial p}{\partial x} + \frac{\partial \tau_{xx}}{\partial x} + \frac{\partial \tau_{yx}}{\partial y} + \frac{\partial \tau_{zx}}{\partial z} + \rho f_x. \qquad (5)$$

In a similar fashion, the *y* and *z* components can be obtained as:

$$\rho \frac{Dv}{Dt} = -\frac{\partial p}{\partial y} + \frac{\partial \tau_{xy}}{\partial x} + \frac{\partial \tau_{yy}}{\partial y} + \frac{\partial \tau_{zy}}{\partial z} + \rho f_y, \qquad (6)$$

$$\rho \frac{Dw}{Dt} = -\frac{\partial p}{\partial z} + \frac{\partial \tau_{xz}}{\partial x} + \frac{\partial \tau_{yz}}{\partial y} + \frac{\partial \tau_{zz}}{\partial z} + \rho f_z. \qquad (7)$$

Equations (5-7) are scalar form of Navier-Stokes equations. One can obtain those Navier-Stokes equations in divergence form as follows.

Writing the left-hand side of equation (5) in terms of the definition of the material derivative [21]:

$$\rho \frac{Du}{Dt} = \rho \frac{\partial u}{\partial t} + \rho \vec{u} \cdot \nabla u. \qquad (8)$$

Also, expanding the following derivative,

$$\frac{\partial (\rho u)}{\partial t} = \rho \frac{\partial u}{\partial t} + u \frac{\partial \rho}{\partial t}. \qquad (9)$$

Recalling the vector identity for the divergence of the product of a scalar times a vector, we have:

$$\nabla \cdot (\rho u \vec{u}) = u \nabla \cdot (\rho \vec{u}) + (\rho \vec{u}) \cdot \nabla u. \qquad (10)$$

Using equations (8-10) we can get:

$$\rho \frac{Du}{Dt} = \frac{\partial (\rho u)}{\partial t} - u \left(\frac{\partial \rho}{\partial t} + \nabla \cdot (\rho \vec{u}) \right) + \nabla \cdot (\rho u \vec{u}). \qquad (11)$$

The term in brackets in equation (11) is simply the left hand side of the continuity equation given as equation (3) hence the term in brackets is zero. Thus equation (11) reduces to:

$$\rho \frac{Du}{Dt} = \frac{\partial (\rho u)}{\partial t} + \nabla \cdot (\rho u \vec{u}). \qquad (12)$$

By substituting equation (12) into equation (5) and transforming using similar fashion equations (6) and (7), the Navier-Stokes equations in conservation (divergence) form can be expressed as:

$$\frac{\partial(\rho u)}{\partial t}+\nabla\cdot(\rho u\vec{u})=-\frac{\partial p}{\partial x}+\frac{\partial\tau_{xx}}{\partial x}+\frac{\partial\tau_{yx}}{\partial y}+\frac{\partial\tau_{zx}}{\partial z}+\rho f_x, \quad (13)$$

$$\frac{\partial(\rho v)}{\partial t}+\nabla\cdot(\rho v\vec{u})=-\frac{\partial p}{\partial y}+\frac{\partial\tau_{xy}}{\partial x}+\frac{\partial\tau_{yy}}{\partial y}+\frac{\partial\tau_{zy}}{\partial z}+\rho f_y, \quad (14)$$

$$\frac{\partial(\rho w)}{\partial t}+\nabla\cdot(\rho w\vec{u})=-\frac{\partial p}{\partial z}+\frac{\partial\tau_{xz}}{\partial x}+\frac{\partial\tau_{yz}}{\partial y}+\frac{\partial\tau_{zz}}{\partial z}+\rho f_z. \quad (15)$$

In the majority of practical aerodynamic problems, the fluid can be assumed to be Newtonian (shear stress in the fluid is proportional to the time-rate-of-strain). For such fluids the expressions for viscous stress terms can be shown as follows [21]:

$$\tau_{ij}=\begin{bmatrix} \lambda\nabla\cdot\vec{u}+2\mu\frac{\partial u}{\partial x} & \mu\left(\frac{\partial v}{\partial x}+\frac{\partial u}{\partial y}\right) & \mu\left(\frac{\partial u}{\partial z}+\frac{\partial w}{\partial x}\right) \\ \mu\left(\frac{\partial v}{\partial x}+\frac{\partial u}{\partial y}\right) & \lambda\nabla\cdot\vec{u}+2\mu\frac{\partial v}{\partial y} & \mu\left(\frac{\partial w}{\partial y}+\frac{\partial v}{\partial z}\right) \\ \mu\left(\frac{\partial u}{\partial z}+\frac{\partial w}{\partial x}\right) & \mu\left(\frac{\partial w}{\partial y}+\frac{\partial v}{\partial z}\right) & \lambda\nabla\cdot\vec{u}+2\mu\frac{\partial w}{\partial z} \end{bmatrix} \quad (16)$$

where μ is the molecular viscosity coefficient and λ is the bulk viscosity coefficient. According to Stokes hypothesis λ= -2μ/3. Substituting the stresses from equation (16) into equations (13-15), one can obtain the complete Navier-Stokes equations for viscous and compressible fluid as follows:

$$\frac{\partial(\rho u)}{\partial t}+\frac{\partial(\rho u^2)}{\partial x}+\frac{\partial(\rho uv)}{\partial y}+\frac{\partial(\rho uw)}{\partial z}=-\frac{\partial p}{\partial x}+\frac{\partial}{\partial x}\left(\lambda\nabla\cdot\vec{u}+2\mu\frac{\partial u}{\partial x}\right)$$
$$+\frac{\partial}{\partial y}\left[\mu\left(\frac{\partial v}{\partial x}+\frac{\partial u}{\partial y}\right)\right]+\frac{\partial}{\partial z}\left[\mu\left(\frac{\partial u}{\partial z}+\frac{\partial w}{\partial x}\right)\right]+\rho f_x, \quad (17)$$

$$\frac{\partial(\rho v)}{\partial t}+\frac{\partial(\rho uv)}{\partial x}+\frac{\partial(\rho v^2)}{\partial y}+\frac{\partial(\rho vw)}{\partial z}=-\frac{\partial p}{\partial y}+\frac{\partial}{\partial y}\left(\lambda\nabla\cdot\vec{u}+2\mu\frac{\partial v}{\partial y}\right)$$
$$+\frac{\partial}{\partial x}\left[\mu\left(\frac{\partial v}{\partial x}+\frac{\partial u}{\partial y}\right)\right]+\frac{\partial}{\partial z}\left[\mu\left(\frac{\partial w}{\partial y}+\frac{\partial v}{\partial z}\right)\right]+\rho f_y, \quad (18)$$

$$\frac{\partial(\rho w)}{\partial t}+\frac{\partial(\rho uw)}{\partial x}+\frac{\partial(\rho vw)}{\partial y}+\frac{\partial(\rho w^2)}{\partial z}=-\frac{\partial p}{\partial z}+\frac{\partial}{\partial z}\left(\lambda\nabla\cdot\vec{u}+2\mu\frac{\partial w}{\partial z}\right)$$
$$+\frac{\partial}{\partial x}\left[\mu\left(\frac{\partial u}{\partial z}+\frac{\partial w}{\partial x}\right)\right]+\frac{\partial}{\partial y}\left[\mu\left(\frac{\partial v}{\partial y}+\frac{\partial v}{\partial z}\right)\right]+\rho f_z. \quad (19)$$

2.3 RANS equations

Since the flow around the train in our particular problem is assumed to be incompressible, it is important to express the continuity and Navier-Stokes equations for incompressible flow (in indices notation) as follows:

$$\frac{\partial u_i}{\partial x_i}=0, \quad (20)$$

$$\rho\frac{\partial u_i}{\partial t}+\rho u_j\frac{\partial u_i}{\partial x_j}=-\frac{\partial p_i}{\partial x_i}+\frac{\partial}{\partial x_j}\left[\mu\left(\frac{\partial u_j}{\partial x_i}+\frac{\partial u_i}{\partial x_j}\right)\right]+\rho f_i. \quad (21)$$

Equations (20) and (21) form a system of four equations with four unknowns. Those are the three velocity components u_i and the pressure p. These equations are nonlinear partial differential equations, which means that there is no analytical solution for the problem with arbitrary boundary conditions. Instead, the flow around the train is solved numerically by discretizing the equations. Depending on the behavior of the flow, different models can be used. The flow around a high speed train becomes turbulent very soon, only a few centimeters after the front part.

The Direct Numerical Simulation (DNS) of turbulent flow using very fine mesh and very small time step is used to resolve the smallest turbulent phenomena and the fastest fluctuations. This approach is capable of resolving turbulence without additional modeling. Eventhough DNS is the most reliable method, resolving turbulence for high Reynolds-number in complex geometries using this method is too computationally expensive. Therefore turbulence needs to be modeled. At present, feasible modeling technologies are steady and unsteady RANS methods, large eddy simulation (LES) and detached eddy simulation (DES).

The method used in the simulation of this study is unsteady RANS model which is based on the decomposition of the flow parameters into a time averaged and a fluctuating component.

Substituting the Reynolds decomposed velocities $u_i=\bar{u}_i+u'_i$ and pressure, $p_i=\bar{p}_i+p'_i$ into equation (20) and (21), and taking the time average (noting that the time-averaged fluctuating parts equals zero and neglecting gravity) one can get the time averaged turbulent flow continuity and RANS equations as follows:

$$\frac{\partial\bar{u}_i}{\partial x_i}=0, \quad (22)$$

$$\frac{\partial\bar{u}_i}{\partial t}+\bar{u}_j\frac{\partial\bar{u}_i}{\partial x_j}=-\frac{1}{\rho}\frac{\partial\bar{p}_i}{\partial x_i}+\frac{\partial}{\partial x_j}\left(\mu\frac{\partial\bar{u}_i}{\partial x_j}-\rho\overline{u'_i u'_j}\right). \quad (23)$$

2.4 Turbulence model

The last nonlinear term in equation (23) is the turbulent stress tensor and can be expressed as:

$$\tau'_{ij}=-\rho\begin{bmatrix} \overline{u'^2} & \overline{u'v'} & \overline{u'w'} \\ \overline{v'u'} & \overline{v'^2} & \overline{v'w'} \\ \overline{w'u'} & \overline{w'v'} & \overline{w'^2} \end{bmatrix}. \quad (24)$$

The need for additional equations to specify these new unknowns is called Turbulence Modeling. To model this stress tensor in terms of the mean flow quantities, and hence provide closure of the above open set of governing equations, the two-equation eddy viscosity model, specifically the realizable k-epsilon turbulence model, is used in our particular problem.

In linear eddy-viscosity models [22-23], the eddy viscosity is derived from turbulent transport equations. One assumes that the turbulent stress is proportional to the mean rate of strain (see equation 25) in a manner similar to viscous stress.

$$ -\rho \overline{u'_i u'_j} = \mu_t \left(\frac{\partial \overline{u}_i}{\partial x_j} + \frac{\partial \overline{u}_j}{\partial x_i} \right) \quad (25) $$

where μ_t is called eddy viscosity or turbulent viscosity (a property that varies with the flow). One can also define a kinematic turbulent viscosity as $\nu_t = \mu_t/\rho$. Equation (25) can be expressed in a more complete form as follows:

$$ -\rho \overline{u'_i u'_j} = \mu_t \left(\frac{\partial \overline{u}_i}{\partial x_j} + \frac{\partial \overline{u}_j}{\partial x_i} \right) - \frac{2}{3} \delta_{ij} (\mu_t \frac{\partial \overline{u}_k}{\partial x_k} - \rho k) \quad (26) $$

where k is the mean turbulent kinetic energy.

The k-epsilon model takes mainly into consideration how the turbulent kinetic energy is affected. In this model, turbulent viscosity is modelled as $\mu_t = \rho C_\mu k^2/\varepsilon$ where, C_μ is a constant, k is the turbulent kinetic energy and ε is the rate of dissipation of turbulent kinetic energy. The realizable k-epsilon model has been widely used in various types of flow simulation. The transport equations for realizable k-epsilon [22-24] model can be expressed as:

$$ \rho \frac{\partial k}{\partial t} + \rho \overline{u}_j \frac{\partial k}{\partial x_j} = \frac{\partial}{\partial x_j} \left[(\mu + \frac{\mu_t}{\sigma_k}) \frac{\partial k}{\partial x_j} \right] + P_k - \rho \varepsilon \quad (27) $$

$$ \rho \frac{\partial \varepsilon}{\partial t} + \rho \overline{u}_j \frac{\partial \varepsilon}{\partial x_j} = \frac{\partial}{\partial x_j} \left((\mu + \frac{\mu_t}{\sigma_\varepsilon}) \frac{\partial \varepsilon}{\partial x_j} \right) + \rho C_1 S \varepsilon - \rho C_2 \frac{\varepsilon^2}{k + \sqrt{\nu \varepsilon}} \quad (28) $$

$$ P_k = -\rho \overline{u'_i u'_j} \frac{\partial u_i}{\partial x_j}, C_1 = \max(0.43, \frac{\eta}{\eta + 5}), $$

$$ \eta = S \frac{k}{\varepsilon} \quad (29) $$

$$ S = \sqrt{2 S_{i,j} S_{i,j}}, \quad S_{i,j} = \frac{1}{2} \left(\frac{\partial \overline{u}_j}{\partial x_i} + \frac{\partial \overline{u}_i}{\partial x_j} \right) \quad (30) $$

The terms on left hand side of equations (27) and (28) present the local rate of change of k and ε and transport of k and ε by convection respectively. Whereas the terms on the right hand side present the transport of k and ε by diffusion, rate of production of k and ε and rate of destruction of k and ε respectively. The model constants (closure coefficients) are $C_\mu=0.09$, $C_2=1.9$, $\sigma_k=1.0$ and $\sigma_\varepsilon=1.2$.

3. NUMERICAL SIMULATION METHOD

In a similar fashion to the experimental set up, the numerical simulation scenario consists of a stationary train exposed to a constant cross wind of 70m/s at different yaw angles ranging from -30° to 60°. For the numerical simulations the commercial CFD software ANSYS FLUENT was used. The detailed numerical simulation procedure such as the model train and computational domain creation, the mesh and boundary conditions are disccused below.

3.1 Definition of coordinate system and aerodynamic coefficients

A definition of the coordinate system is given in Fig.5.
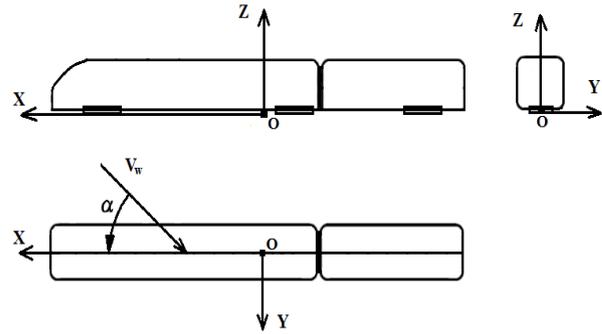
Fig.5. Definition of coordinate system and yaw angle (α)

The non-dimensionalized aerodynamic side force coefficient (C_s) and rolling moment coefficient (C_m) can be calculated as follows:

$$ Cs = \frac{F_y}{0.5 \rho V_w^2 A} \quad (31) $$

$$ C_{mx} = \frac{M_x}{0.5 \rho V_w^2 AL} \quad (32) $$

where F_y is the force in the y direction, M_x is the moment about x-axis, ρ is the air density, V_w denotes the approaching air speed, A represents a fixed reference area and L represents a fixed reference length.

3.2 Description of the model geometry

Full-size trains are not often used for aerodynamic studies owing to their geometrical complexities; instead, simplified, shortened models are used. Performing numerical simulation for a complete train with a length of about 205m requires more advanced computational resources than those available. In addition, since the flow structure downstream of a certain distance from the nose of the train (less than one coach length) is more or less constant, a decrease in length does not alter the essential physical features of the flow [25].

The model studied in this work is a more realistic version of the ICE-2 high speed train which consists of the leading car, end car and inter-car gap. The model geometry has total length of 29.3m, width of 3m and height of 3.9m. The model has been created with simplified bogies as shown in Fig. 6.
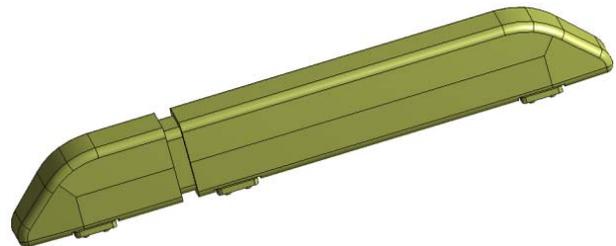

Figure 6. Leading and end car model with simplified bogie used in the numerical simulation

The moment reference point is set to be located at ground level in the midway of the train length. The

coefficients for the aerodynamic forces and moments have been obtained using a fixed reference area of 11.6m^2 which corresponds to the cross-sectional area of the train model and reference length of 3m which presents the width of the train model.

3.3 Computational domain and mesh

After the basic shape of the train has been created, a parallelepiped computational domain (Fig. 7) of the following dimensions: height 50m, width 100m and length 150m is created simulating the wind tunnel working section. In the computational domain, the model can be rotated in the x-y plane by the required yaw angle for simulation. The distance between nose of vehicle and the inlet boundary is around 50m which is sufficient to ensure that the velocity and pressure fields are uniform at the inlet and to allow the flow to develop by the time it reaches the train. The model is also sufficiently far from the top and side walls to minimize near wall effects.
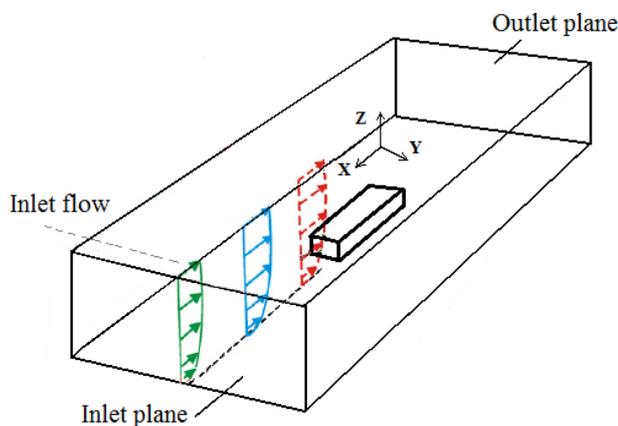
Figure 7. Computational domain with a train model for CFD simulation

The mesh of the computational domain was generated using a tetrahedron patch conforming method. Mesh refinement has been done on the train surfaces, bogies of the train and areas surrounding the train. The generated mesh consists of 3,127,697 elements. The mesh resolution at the wall is very important. For standard or non-equilibrium wall functions, each wall-adjacent cell's centroid should be located within the log-law layer, $30<y^+<300$. In the generated meshes, five prismatic cell layers of constant thickness were made on the train walls and the first cell layer adjacent to the walls of the train was adjusted to meet the requirements of y^+. The cross-section of the meshes with refinement on the modeled train surfaces and surrounding areas is shown in Fig. 8.
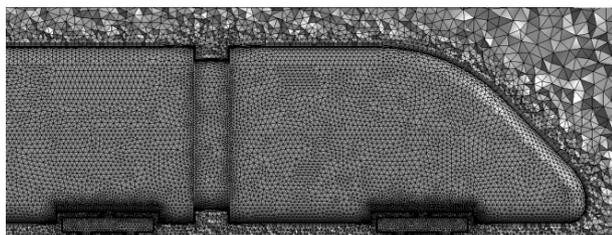
Figure 8. Cross section of the mesh

3.4 Boundary condition

The flow enters the domain with a uniform velocity of 70m/s. The Reynolds number based on the inlet flow velocity and the width of train model was 1.4×10^7. No-slip boundary conditions were used on the train surface and the ground floor meaning that the velocity is zero. Symmetry boundary conditions were used on the top and side walls.

On the outlet, a uniform Neumann boundary condition is applied, meaning that the pressure gradient equals zero. This allows the flow to pass through the outlet without affecting the upstream flow, provided that the upstream distance to the aerodynamic body is large enough. The realizable k-epsilon model was used for the turbulence closure.

The inflow turbulence intensity and length scale were set to be 3% and 0.3m respectively. On the ground and solid surfaces, the non-equilibrium wall functions were used to determine the boundary turbulence quantities. All runs were performed in a transient mode with a time step of 0.08 sec, which was considered small enough to resolve the fluctuations in the aerodynamic forces.

The conventional SIMPLE algorithm was used to solve the coupled equations, where several iterations are performed in each time step to ensure convergence.

4. RESULTS AND DISCUSSIONS

Convergence is achieved when both the side force and rolling moment deviate less than 0.01% in conjunction with residuals that are nearly fully converged. The computed coefficients of side force and rolling moment were compared to experimental data and shown in Fig. 9 and 10 respectively [14].

As can be seen in the graphs, the computed side force and rolling moment coefficients are in good agreement with the experimental data. However, at yaw angles of 40° and 50° CFD slightly under-predicts the side force and over-predicts the rolling moment. This may be due to the effect of inter car gap that was included in the CFD model.

The nature of the flow field and its structures is depicted by contours of velocity vectors, total pressure distributions and streamline patterns along the train's cross-section are presented in Fig. 11-16. As expected, for large yaw angles, large flow separation zone and lower pressure region exist on the leeward side of the train.

4.1 Side force coefficient

As can be seen from Fig. 9, the side force coefficient increases steadily with yaw angle till about 50° before it starts to exhibit an asymptotic behavior. Side force is mainly caused by the pressure difference on the two sides of the train.

The side force increases the wheel-track load on the leeward side and the wheel-rail contact force.

Large side forces worsen the wear of the wheel and rail, and may cause train derailment, or even overturning.
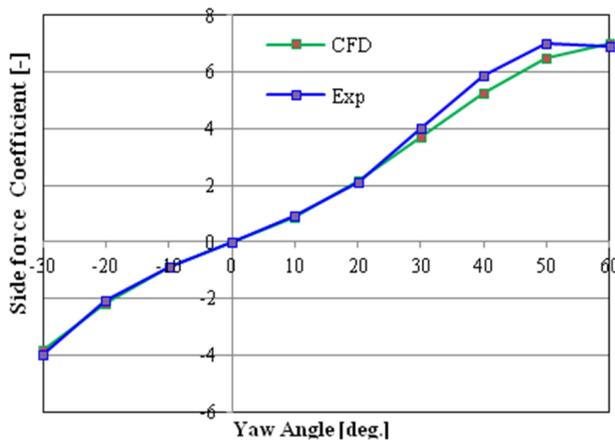
Figure 9. Side force coefficient vs. yaw angle

4.2 Rolling moment coefficient

As can be seen from Fig.10, the rolling moment coefficient varies in a similar fashion to the side force and the result is in a good agreement with the experiment. The rolling moment is the result of both the lift and side forces with the side force being the main contributor. The rolling moment is responsible for the overloading of wheel-track on the leeward side and is found to be one of the most important aerodynamic coefficients regarding cross-wind stability.
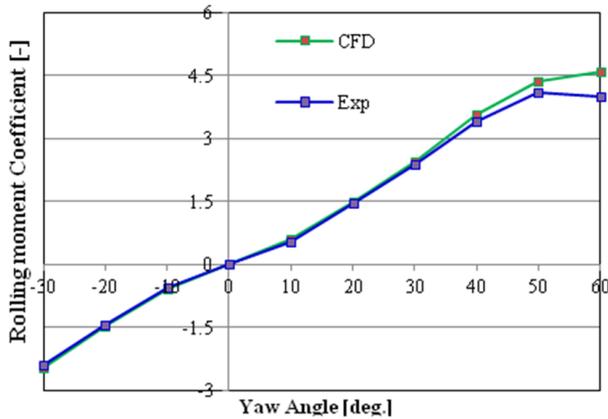
Figure 10. Rolling moment coefficient vs. yaw angle

4.3 Flow structure

The flow structure for different yaw angles is shown in detail by the two-dimensional streamlines at different locations on the x-axis in Fig. 11 and 12. As can be seen from the figures, flow separation takes place on both the lower and upper leeward edges and the vortex distribution depends on the yaw angle. The recirculation region caused by the vortex flow starts bieng adjacent to the walls of the train, then it slowly drifts away from the surface as the flow develops further towards the wake. Contours of velocity vectors and total pressure distributions (Fig.13-16) have been computed at different cross-sections from the nose of the train along its length for different yaw angles. As can be seen in Fig. 13 and 14, the flow accelerates in the train's top surface and the gap between the ground and the train's bottom surface. Due to the presence of vortex on the

leeward side, a low pressure region is created (Fig. 15 and 16). The existence of the lower pressure region on the leeward side of the train explains the increased side force and roll moment.
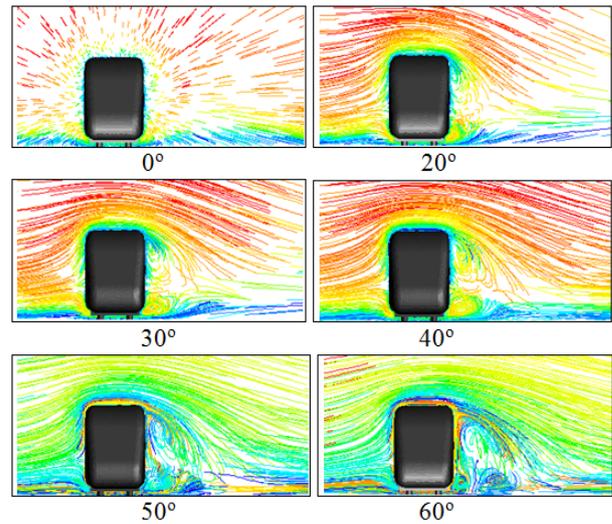

Figure 11. Mean streamlines along the train's cross section at 4.15m from the nose of the train
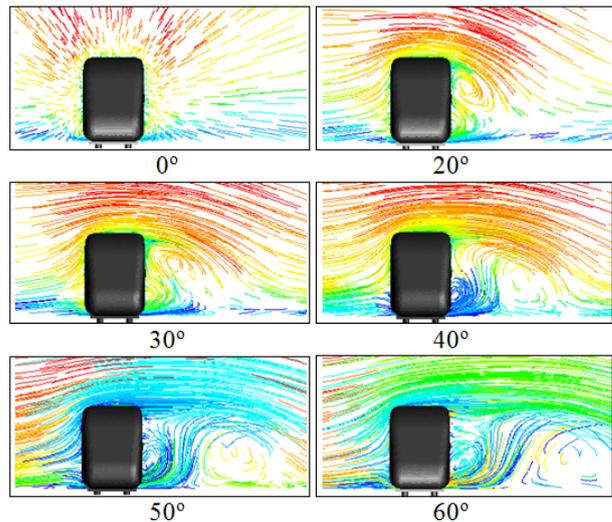

Figure 12. Mean streamlines along the train's cross section at 14.65m from the nose of the train
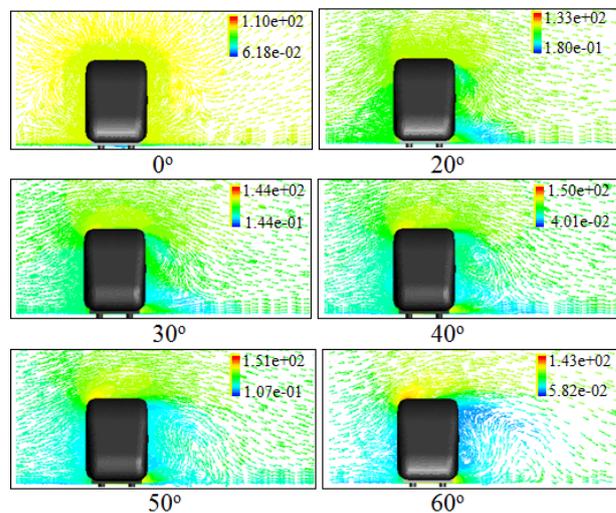

Figure 13. Velocity vectors along the train's cross section at 9.65m from the nose of the train coloured by velocity magnitude (m/s)
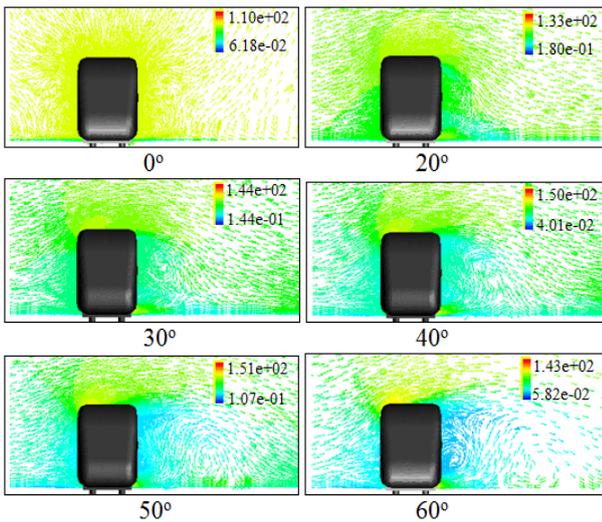
Figure 14. Velocity vectors along the train's cross section at 14.65m from the nose of the train coloured by velocity magnitude (m/s)
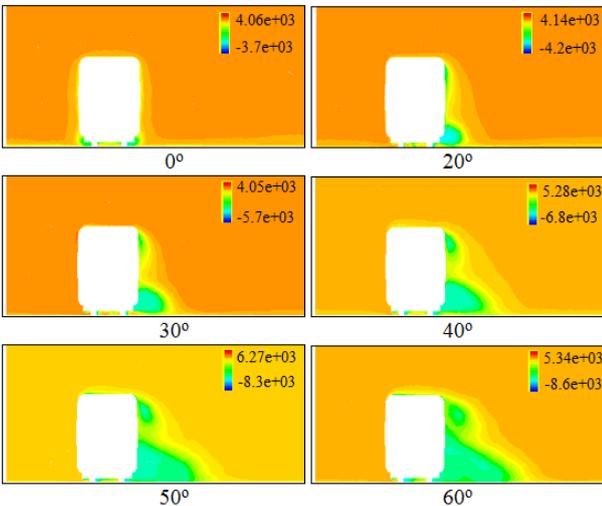

Figure 15. Total pressure contours (in pascal) along the train's cross section at 4.15m from the nose of the train
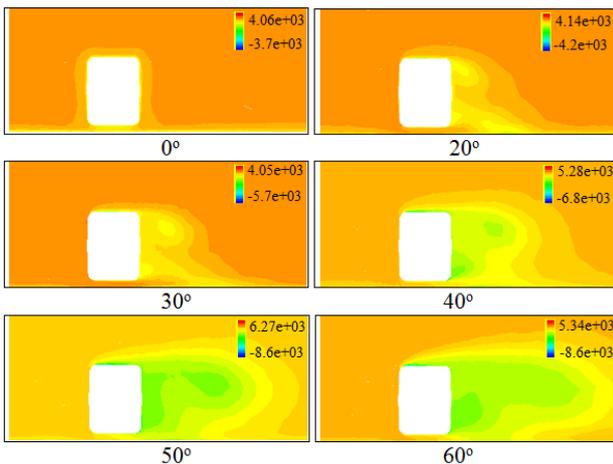

Figure 16. Total pressure contours (in pascal) along the train's cross section at 14.65m from the nose of the train

The pressure coefficient around the circumference of the train at different locations along its length is plotted in Fig.17 for yaw angle of 60°. As can be seen from graphs the pressure distribution does not change much along the train length except in a small region close to the nose. This shows that the pressure distribution

around a high speed train at higher yaw angles is almost independent on the axial position.
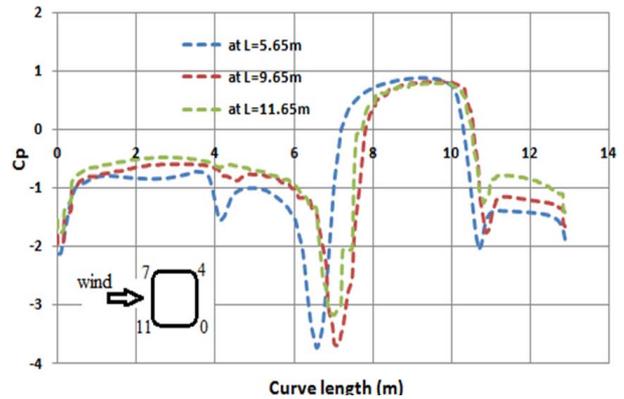

Figure 17. Pressure coefficient along the train's cross section at different distance (L) from the nose of the train

5. CONCLUSION

The flow of turbulent cross wind over a more realistic ICE-2 high speed train model has been simulated numerically by solving the unsteady three dimensional RANS equations. The simulation has been done in static ground case scenario for different yaw angles. The computed aerodynamic coefficient outcomes using the realizable k-epsilon turbulence model were in good agreement with the experimental data for almost all yaw angles. This study shows that unsteady CFD-RANS methods combined with an appropriate turbulence model can present an important means of assessing the crucial aerodynamic forces and moments of a high speed train under cross wind conditions. The aerodynamic data obtained in this study can be used as a starting point for more advanced studies that investigate influence of strong cross wind on the aerodynamic coefficients of high speed trains while moving either on flat ground or in other dangerous scenarios such as sites with tall viaducts and high embankments.

REFERENCES

[1] Zhou, L. and Shen, Z.: Progress in high-speed train technology around the world, Journal of Modern Transportation, Vol. 19, No. 1, pp. 1-6, 2011.

[2] Baker, C.J.: Measurements of the cross wind forces on trains, Journal of Wind Engineering and Industrial Aerodynamics, Vol. 92, pp. 547-563, 2004.

[3] Blakeney, A.: *Resistance of railway vehicles to roll-over in gales*, Railway group standard, Safety & Standards Directorate, Railtrack PLC, London, 2000.

[4] Mancini, G., Cheli, R., Roberti, R., Diana, G., Cheli, F. and Tomasini, G.: Cross-wind aerodynamic forces on rail vehicles wind tunnel experimental tests and numerical dynamic analysis, in: *Proceedings of the World Congress on Railway Research*, 28.09-01.10.2003, Edinburgh, pp. 513-522.

[5] DB Netz AG: *Ril 80704: Aerodynamik/ Seitenwind*, DB Netz AG, Frankfurt a.M., 2006. (in German)

[6] *EC.TSI-Technical Specification for Interoperability of the trans-European high speed rail system*, European Law, Official Journal of the European Communities, 2006.

[7] *CEN: EN 14067-6:2010 Railway applications Aerodynamics Part 6: Requirements and test procedures for crosswind assessment*, CEN, European Committee for Standardization, Brussels, 2010.

[8] Elisa, M. (Ed.) and Hoefener, L. (Ed.): *Aerodynamics in the open air (AOA), WP2 Cross Wind Issues,* Final Report, DeuFraKo Project, Paris, 2008.

[9] Diedrichs, B.: Aerodynamic calculations of cross wind stability of a high-speed train using control volumes of arbitrary polyhedral shape, in: *VI International Colloquium on: Bluff Bodies Aerodynamics & Applications (BBAA)*, 20-24.07.2008, Milan, CWT-01.

[10] Carrarini, A.: Reliability based analysis of the crosswind stability of railway vehicles, Journal of Wind Engineering and Industrial Aerodynamics Vol. 95, pp. 493-509, 2007.

[11] Kwon, H., Park, Y., Lee, D. and Kim, M.: Wind tunnel experiments on Korean high-speed trains using various ground simulation techniques, Journal of Wind Engineering and Industrial Aerodynamics, Vol. 89, pp. 1179–1195, 2001.

[12] Baker, C.J.: The wind tunnel determination of crosswind forces and moments on a high speed train, Notes on Numerical Fluid Mechanics, Vol. 79, pp. 46–60, 2002.

[13] Bocciolone, M., Cheli, F., Corradi, R., Diana, G. and Tomasini, G.: Wind tunnel tests for the identification of the aerodynamic forces on rail vehicles, in: *XI ICWE-International Conference on Wind Engineering*, 2-5.06.2003, Lubbock.

[14] Orellano, A. and Schober, M.: Aerodynamic Performance of a Typical High-Speed Train, in: *Proceedings of the 4th WSEAS International Conference on Fluid Mechanics and Aerodynamics*, 21-23.08.2006, Elounda, pp. 18-25.

[15] Cheli, F., Corradi, R., Rocchi, D., Tomasini, G. and Maestrini, E.: Wind tunnel test on train scaled models to investigate the effect of infrastructure scenario, in: *VI International Colloquium on: Bluff Bodies Aerodynamics & Applications* (*BBAA)*, 20-24.07.2008, Milan, TRENI.POLIMI-2.

[16] Cheli, F., Ripamonti, F., Rocchi, D. and Tomasini, G.: Aerodynamic behaviour investigation of the new EMUV250 train to cross wind, Journal of Wind Engineering and Industrial Aerodynamics Vol. 98, pp. 189-201, 2010.

[17] Krajnovic, S., Ringqvist, P., Nakade, K. and Basara, B.: Large eddy simulation of the flow around a simplified train moving through a crosswind flow, Journal of Wind Engineering and

Industrial Aerodynamics, Vol. 110, pp. 86-99, 2012.

[18] Guilmineau, E., Chikhaoui, O., Deng, G. and Visonneau, M.: Cross wind effects on a simplified car model by a DES approach, Computers & Fluids Vol. 78, pp. 29-40, 2013.

[19] Wendt, J.F.: *Computational Fluid Mechanics: An Introduction*, Springer-Verlag, Berlin Heidelberg, 2009.

[20] Currie, I.G.: *Fundamental Mechanics of Fluids*, McGraw-Hill, New York, 1974.

[21] Blazek, J.: *Computational Fluid dynamics: Principles and applications*, Elsevier Science Ltd, Oxford, 2001.

[22] Wilcox, D.C.: *Turbulence Modelling for CFD*, 3rd edition, DCW Industries, Inc., La Canada, 2006.

[23] Schlichting, H. and Gersten, K.: *Boundary layer theory*, Springer-Verlag, New York, 1999.

[24] Celik, I.B.: *Introductory Turbulence Modeling*, Lecture Notes, West Virginia University, Morgantown, 1999.

[25] Khier, W., Breuer, M. and Durst, F.: Flow structure around trains under side wind conditions: a numerical study, Computers & Fluids, Vol. 29, pp. 179-195, 2000.

АЕРОДИНАМИЧКЕ КАРАКТЕРИСТИКЕ ВОЗОВА ВЕЛИКИХ БРЗИНА ПОД ДЕЈСТВОМ БОЧНИХ ВЕТРОВА: НУМЕРИЧКА АНАЛИЗА КОРИСТЕЋИ НЕСТАЦИОНАРНИ RANS МЕТОД

Assress Mulugeta Biadgo, Александар Симоновић, Јелена Сворцан, Слободан Ступар

Услед тренда повећања брзина и смањења масе модерних возова великих брзина неопходно је разматрати дејство јаких бочних ветрова на њихову аеродинамику. Јаки бочни ветрови могу утицати на стабилност ових возова услед повећања аеродинамичке силе и момента. У овој анализи спроведене су нумеричке симулације турбулентних бочних ветрова који дувају преко првог и последњег вагона брзог воза ICE-2 при различитим угловима скретања. Проблеми стабилности воза су блиско везани за струјно поље око воза. Околни флуид сматран је нестишљивим, а струјно поље око воза добијено је решавањем нестационарних Рејнолдсових једначина (RANS) у комбинацији са realizable k-epsilon турбулентним моделом. Аеродинамички коефицијенти важни за ову анализу, коефицијент силе клизања и момента скретања, израчунати су за углове скретања у опсегу од -30° до 60° и упоређени са резултатима добијеним у аеротунелу. Квалитативна анализа зависности струјних структура од угла скретања је такође спроведена и приказана.